PneuNet actuators design: Trade-offs between deformation, force, and resistance to buckling

Zeinab Awada, Yassine Haddab, Marc Gouttefarde

PneuNet Actuators Design: Trade-offs between Deformation, Force, and Resistance to Buckling

Zeinab Awada[a,*], Yassine Haddab[a] and Marc Gouttefarde[a]

[a]*LIRMM, Univ Montpellier, CNRS, Montpellier, France*

ARTICLE INFO

Keywords:
Soft robotics
Soft pneumatic actuators
Soft bending actuator
Design optimization
Soft grippers

ABSTRACT

Soft pneumatic network (PneuNet) actuators and their derived grippers have gained prominence in industrial and medical applications. The performance of PneuNets is typically assessed based on their angular deformation and the tip force they exert. To enhance their effectiveness, several studies have investigated the relationship between design parameters and these critical performance metrics. This paper expands upon existing literature by examining the impact of design parameters on three performance metrics: angular deformation, tip force, and resistance to buckling—the latter proposed for the first time as a performance metric for PneuNets. Resistance to buckling is significant in applications requiring high forces with minimal restrictions on maximum allowable pressure. The angular deformation and tip force are analyzed by introducing additional design parameters previously unexplored in the literature. Moreover, the former is studied in three different configurations. In this context, the configuration of the PneuNet actuator refers to its orientation, such as horizontal or vertical fixation, and whether it bends against or towards gravity. These configurations simulate environmental factors and the diverse positions that PneuNets may encounter in practical applications. It is demonstrated that the influence of some design parameters on angular deformation is configuration-dependent. Furthermore, a comprehensive table is provided to aid users in optimizing PneuNet performance—whether in terms of angular deformation, tip force, or resistance to buckling—according to specific application requirements. Finally, to evaluate the practical applications of these performance metrics, five PneuNet grippers with different shapes are fabricated and tested in two distinct gripping modes.

1. Introduction

To address recent challenges, robotic performance has been redefined by substituting rigidity with intrinsic compliance and precision with adaptability [1]. This new approach is partially implemented in rigid robots by replacing rigid joints with flexible ones, thereby enhancing the compliance of these structures [2]. Later on, compliance and adaptability has been extended and eventually embodied by soft robots. Soft robots 'gently' navigate and manipulate their environment by adapting to its features, leveraging their inherent compliance. Though it comes at the cost of reducing the exerted forces, this morphing capability is indispensable for a number of tasks performed in confined places or for agricultural [3] and medical [4] applications.

In the realm of agriculture and with the pressing concern of an impeding food crisis [5], efforts have been made to automate the harvesting process. This raises the challenge of designing a gripper that is delicate to preserve corps yet forceful enough to maintain a tight grip. For this purpose, a soft gripper, similar to that shown in Fig. 1, has been proposed [6–13]. Inspired by the human hand, it has three or more pneumatical 'finger-like' actuators called pneumatic networks (PneuNets). Having air chambers connected by a canal, PneuNets are soft actuators that bend under pressure [14, 15].

Besides their success in soft grippers, PneuNets inspire the design of complex bending mechanisms [16], and their performance is characterized by their bending angle and the force generated at their tip [6–11, 13, 17–21]. However, due to their soft nature, PneuNets exert lower output forces compared to their rigid counterparts. Consequently, a significant challenge arises in increasing the output forces of PneuNets without compromising their angular deformation. Existing literature addresses this challenge through two primary approaches. The first approach involves innovative redesigns of PneuNet structures, starting from classical designs to create new configurations that produce higher forces [18, 22]. Examples include connecting two PneuNets in series [9, 23], each with its own air inlet, winding copper coils around the PneuNet chambers [19], or integrating tendon actuation [13]. Conversely, the second approach adopts a more

*Corresponding author
zeinab.awada@lirmm.fr (Awada)

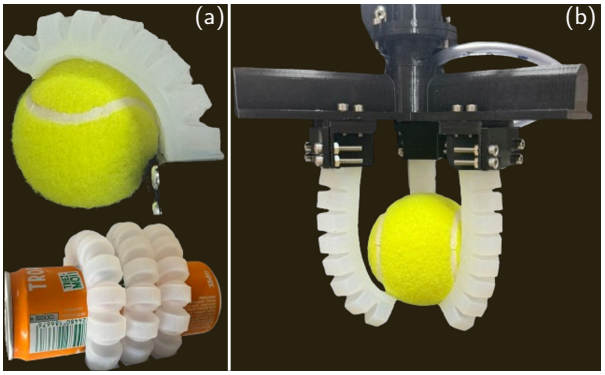

Figure 1: Two grasping modes are shown: (a) The gripper seizes a tennis ball (top) and a can (bottom) by enveloping them. (b) The gripper grasps a tennis ball using its tips.

fundamental route by revisiting classical PneuNets to analyze how the performance is impacted by various design parameters such as chambers dimensions and total actuator length [6, 12, 17, 20, 23–26]. The latter approach aims to enhance the performance of classical PneuNets before considering more elaborate redesigns.

Owing to the valuable insights it provides, the present work aligns with the second approach. Hence, a comprehensive overview of the specific contributions made by similar studies is given in Table 1. Although the shape of the PneuNet varies across different investigations, a consistent trend emerges regarding the impact of design parameters on performance. In [20, 23–26], researchers predominantly employed PneuNets with rectangular chambers. Conversely, [17] explored a PneuNet design featuring semi-oblong chambers. In [6, 22], chambers with a similar semi-oblong shape were utilized, albeit in a rotated orientation compared to [17].

Across several studies [6, 17, 20, 22–26], roboticists have examined various parameters, including chamber thickness, number, height, width, spacing, PneuNet length, and silicone base thickness, analyzing their effects on actuator performance. For instance, [25] went beyond conventional parameters, examining the influence on the angular deformation of the vertical silicone thickness around connecting canals. Expanding the inquiry, [20, 24] evaluated the angular deformation and tip force of PneuNets having different shapes, as presented in Table 1. Moreover, [6, 22, 23] evaluated the grasping capabilities of PneuNet actuators and grippers by attempting to seize objects of different shapes and masses using the tips as shown in Fig. 1b.

Furthermore, when studying angular deformation, it is important to consider the configuration of the PneuNet, defined by how it is fixed (horizontally or vertically) and the direction it bends (upwards or downwards). This configuration is a significant factor as it reflects environmental conditions and application requirements. Except for [26], which examined the impact of the actuator length on angular deformation in a vertical configuration, all studies in Table 1 considered the PneuNet actuator to be fixed horizontally and bending downwards.

In summary, these studies: (1) Apart from [25] that consider only one canal parameter, overlook the design parameters of connecting canals, which have an important role in the overall performance of the PneuNet actuator [25]. These parameters could significantly affect factors such as fluid flow and pressure distribution within the actuator, ultimately influencing its behavior. (2) Mostly explore one configuration when investigating the impact of design parameters on angular deformation. However, in practical applications, PneuNet actuators may be mounted in various configurations, potentially resulting in different influences of design parameters when combined with gravitational forces. (3) When considering applications involving grippers, tend to conduct experiments limited to a single seizing mode (generally that shown in Fig. 1b), without comparing grippers of different shapes. A more comprehensive approach would include evaluating various seizing modes and comparing the performance of grippers with different shapes, providing valuable insights for practical applications.

The primary contribution of this paper lies in evaluating the impact of design parameters on the PneuNet actuator across three key performance metrics: resistance to buckling, tip force, and angular deformation. While the concept of resistance to buckling is inspired by previous work [27], to the authors' best knowledge, it has not been applied to PneuNet actuators before. Additionally, compared to existing studies, our research introduces additional design parameters and conducts a detailed analysis of their effects on both tip force and angular deformation. Notably, these additional design parameters include the chambers aspect ratio, shape, and orientation, as well as the connecting canal

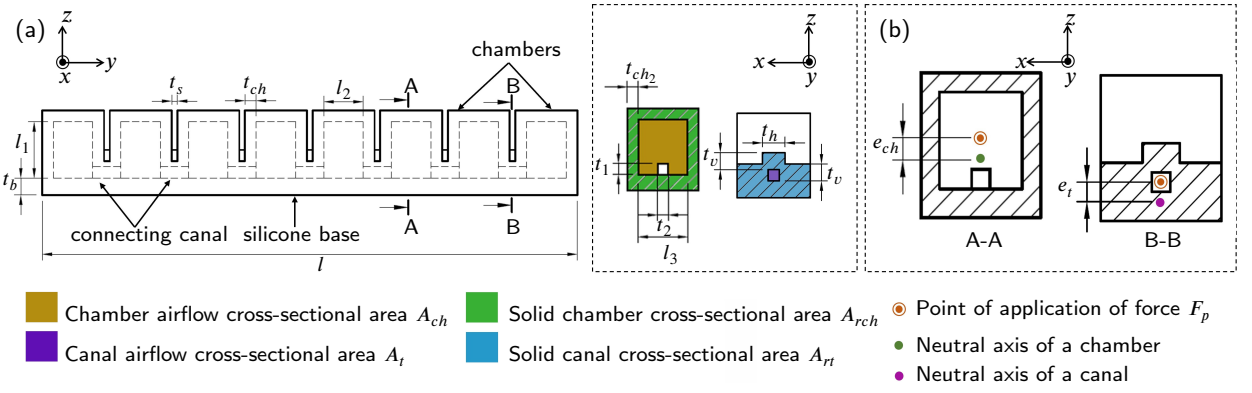

Figure 2: Representation of a rectangular PneuNet: (a) Lateral view showing chambers connected by a canal, with a projected view of both the chamber and the canal. (b) A close-up cross-sectional view of the chamber and canal showing the points of application of F_p, the force generated by the actuation pressure P, with respect to the neutral axes of a chamber and a canal.

length, width, and the silicone thicknesses around it both horizontally and vertically. Furthermore, when studying angular deformation, we examine three distinct configurations: vertically fixed, horizontally fixed and bending downwards, and horizontally fixed and bending upwards. This approach allows us to elucidate how design parameters interact differently across these configurations. Finally, the impact of chamber shape on grasping capabilities was assessed by fabricating five grippers with different shapes and evaluating their performance in the two gripping modes illustrated in Fig. 1.

To study the impact of design parameters, three approaches are possible: model-based, simulation, or experimental. Existing models for angular deformation and tip force either rely on variables requiring experimental or simulation measurements [28, 29] or fail to account for all design parameters [17, 18, 25, 30], making a model-based approach insufficient or impractical. Despite this, an overview of these analytical models is provided in Section 2, as they offer insights into the trends in angular deformation and tip force for some design parameters. Nevertheless, an overview of these models is provided in Section 2, as they offer useful insights into trends for certain design parameters. While FEA provides greater generality than analytical models, discrepancies have been reported between FEA simulation and experimental results. These discrepancies are often related to inaccurately capturing the influence of gravity or to errors in material characterization [16]. Moreover, FEA is computationally intensive for hyperelastic materials like the silicone used in PneuNet actuators, often requiring several hours per simulation depending on the desired accuracy and meshing resolution [31]. Given the need for a comprehensive evaluation across a wide range of design parameters and considering time efficiency, this work adopts an experimental approach. A detailed comparative study between the three approaches is reported in [37]. PneuNet actuators are fabricated using Dragon Skin 10 No Vacuum from Smooth-On, following the traditional molding method described in [6, 23, 30, 32]. The molds are printed with a precision of 0.1 mm using Fortus 400mc (Stratasys, Ltd).

The paper is structured as follows. Section 2 outlines three performance metrics of PneuNet actuators: angular deformation (and the three studied configurations), tip force, and resistance to buckling. Section 3 explores how the impact of previously studied parameters vary with configuration changes and introduces the effects of new design parameters on the performance metrics. Section 4 assesses the gripping capabilities of PneuNet-based grippers. Finally, Section 5 summarizes the key findings of this work, and Section 6 concludes the paper.

2. Performance metrics overview

PneuNet actuators are composed of chambers connected by a canal. To enhance the compliance of the structure, the chambers are separated by gaps of length t_s (Fig. 2a). A silicone base of thickness t_b, which is inherently more resistant to deformation than the chambers and the canal, is positioned beneath them. In some designs, a strain-limiting layer may be embedded within the silicone base to constrain the extension of the actuator. However, in this study, all PneuNet actuators are fabricated without a strain-limiting layer. The decision to omit the strain-limiting layer was motivated by the following considerations:

1. **Simplification of study scope:** This study focuses on the design parameters of the PneuNet actuator itself, excluding additional variables introduced by a strain-limiting layer, such as its material composition, position, and dimensions. By narrowing the scope, we aim to provide a clearer analysis of the intrinsic properties of the actuator.
2. **Fabrication simplicity:** Given that an experimental approach is adopted in this study (as established in the previous section and detailed in [37]]), omitting the strain-limiting layer simplifies the fabrication process by removing the need for precise alignment and placement of the layer.
3. **Generality of findings:** Importantly, the absence of a strain-limiting layer does not compromise the generality of the findings. A comparative study, detailed in the supplementary material [37], demonstrates that actuators with and without a strain-limiting layer exhibit consistent trends in performance metrics, despite some quantitative differences.

To refine the approach to their design optimization, this section presents three key performance metrics of PneuNet actuators: angular deformation, tip force, and resistance to buckling. While this study is the first to investigate the resistance to buckling in PneuNet actuators, several prior works have modeled their angular deformation $\Delta\theta$ and tip force F_t [6, 17, 28, 32, 33]. These models, though primarily developed for actuators with strain-limiting layers, provide valuable insights into the relationships between performance metrics and design parameters. Our comparative study (supplementary material [37]) further validates the applicability of these models to actuators without strain-limiting layers by demonstrating that the fundamental trends in performance remain consistent. The following subsections introduce each performance metric in detail, while Table 2 defines the variables used in this study.

2.1. Angular deformation

High angular deformation is critical for achieving a large workspace and is important for specific applications, such as the gripping mode shown in Fig. 1a. One factor contributing to the bending of the actuator is the contact forces between inflated chambers. The presence and impact of these forces depend on the actuator design—its dimensions and canal position—as well as the specific configuration of the PneuNet, as illustrated in Fig. 3 and further discussed in this subsection.

Another significant factor contributing to the actuator's bending is the moment generated by the actuation pressure P, which is a focus of several studies modeling the angular deformation $\Delta\theta$ [6, 17, 28, 33]. This bending is generated by the geometric asymmetries in the cross-sections of both the chamber and the canal. Specifically, the neutral axis of the chamber cross-section is e_{ch} below its airflow geometric center, while the neutral axis of the canal cross-section is e_t below its airflow geometric center, as depicted in Fig. 2b. Starting from here, the PneuNet actuator is modeled as a cantilevered beam in [28], with its angular deformation described using Euler-Bernoulli beam theory [34]. When internal pressure P is applied to the actuator, a tensile force F_p is generated at the centers of the airflow cross-sections of the canal and chamber, as shown in Fig. 2b. The tensile force F_p creates a bending moment at the chamber and canal cross-sections due to the lever arms e_{ch} and e_t, resulting in moments $F_p \cdot e_{ch}$ and $F_p \cdot e_t$, respectively.

The eccentricities e_{ch} and e_t are calculated by dividing the cross-section into N rectangles, each with an area A_j and a geometric center situated at y_j (j=1, ..., N) with respect to a chosen reference position ($y = 0$) [35]. For a chamber cross-section ($i = ch$) and a canal cross-section ($i = t$), the eccentricities e_{ch} and e_t are calculated using the following equation

$$e_i = d_i - \frac{\sum_{j=1}^{N} A_j y_j}{\sum_{j=1}^{N} A_j} \tag{1}$$

where d_i is the position of the geometric center of the airflow areas of the chamber ($i = ch$) and the canal ($i = t$) with respect to the reference position $y = 0$.

Similar to a cantilevered beam, the angular deformation $\Delta\theta_i$ for a chamber ($i = ch$) and a canal ($i = t$) is given by [28]

$$\Delta\theta_i = \frac{P A_i e_i}{E I_i} k_i \tag{2}$$

In this equation, k_i represents a term that includes the respective lengths and experienced elongations upon actuation, specifically $2t_{ch} + l_2 + \Delta l$ for the chamber and $t_s + \Delta l'$ for the canal.

The total angular deformation $\Delta\theta$ of the actuator is the sum of the angles at the n chambers and $n-1$ canal cross-sections and hence reads

$$\Delta\theta = n\Delta\theta_{ch} + (n-1)\Delta\theta_t \tag{3}$$

In [28], the actuator is fabricated from nonlinear elastomer material and a strain-limiting layer. Due to the nonlinearity of the material and the composite structure, the chamber EI_{ch} and canal EI_t flexural rigidities cannot be estimated but require additional experimental measures to be determined for different pressure ranges.

Several experimental studies support the trends suggested by Eq. 2, indicating that $\Delta\theta$ increases with the number of chambers n [20, 25], as well as the height l_1 [6, 36] and width l_3 [36] of the chambers. Conversely, $\Delta\theta$ decreases with a reduction in the longitudinal t_{ch} [25] and transverse t_{ch_2} [24] thicknesses of the chambers, as well as the space t_s [20, 24, 25] between them. The relationship between $\Delta\theta$ and the bottom silicone thickness t_b is nonlinear and depends on the actuator design [24].

The aforementioned studies primarily consider the PneuNet actuator when it is horizontally suspended and bending downwards, similar to the configuration in Fig. 3d. However, a PneuNet actuator might be mounted in different configurations. This variability is particularly significant in grippers since their orientation depends on the object to be grasped. Therefore, it is pertinent to study whether the impact of design parameters is influenced by the configuration of the actuator. Hereafter three configurations are considered: In configuration 1 (Fig. 3a), the PneuNet is vertically suspended. When pressurized, it bends upwards while progressively carrying its own weight (Fig. 3b-c). In both configurations 2 (Fig. 3d-f) and 3 (Fig. 3g-i), the PneuNet is horizontally suspended. In configuration 2, for low angular deformations, the weight of the PneuNet helps it bend in the direction of gravity (Fig. 3e). However, for larger angular deformations, the weight of the PneuNet becomes disadvantageous to bending (Fig. 3f). The opposite happens in configuration 3. In this case, the chambers are initially in contact (Fig. 3g). Therefore, when under low pressure, the PneuNet bends upward against gravity and the contact forces between the chambers contribute to bending (Fig. 3h). When the PneuNet reaches a sufficiently large angular deformation, the chambers are no longer in contact and the PneuNet bends only due to the bending moment created by the tensile force F_p. In this phase, the weight of the PneuNet progressively favors the angular deformation (Fig. 3i).

Subsection 3.1 looks at how the effect of design parameters can change based on the configuration. Moreover, new design parameters influencing $\Delta\theta$ are investigated in Subsection 3.1.2 to Subsection 3.1.5, including dimensions of the canal (t_1, t_2, t_v, and t_h), aspect ratio of the chamber r, and chamber shapes and orientation. To measure the angular deformation $\Delta\theta$, the free tip of the PneuNet actuator is marked with a red marker for better visibility. The actuator is progressively pressurized, and its deformation is recorded using a 30 frames-per-second camera. A visual tracking algorithm is then applied to calculate the angle between the actuator tip and a reference line: either a vertical line (configuration 1) or a horizontal line (configurations 2 and 3) passing through the fixed end of the actuator. This process is illustrated in Fig. 4a-c.

2.2. Tip force

When blocked by an object at its tip, a tip force F_t is generated such that the equilibrium of torques between the tip force moment, internal bending moment, contact moment between the chambers, and the elastic restoring moment of the silicone is satisfied [25]. A large tip force is particularly important in the grasping mode shown in Fig. 1b. In [29], F_t is modeled by considering a PneuNet actuator with a strain-limiting layer. Its expression reads

$$F_t = \frac{F_c d_{mb}}{l_2 + 2t_{ch} + \frac{t_s}{2}} \cos(\alpha) \tag{4}$$

where α is defined in Fig. 4d, F_c is the contact force between the last two adjacent chambers, and d_{mb} is the distance from the contact point of two adjacent chambers to the strain-limiting layer.

Eq. 4 suggests that F_t decreases with an increase in the length of the chamber l_2 (and hence total length of the actuator l), the chamber longitudinal thickness t_{ch}, and the distance between the chambers t_s. Additionally, several studies find that F_t increases with an increase in the width l_3 [22] and height l_1 [30] of a chamber. Conversely, it decreases with an increase in the chamber cross-sectional thickness t_{ch_2} [22] and the number of chambers n [23].

To avoid redundancy, the above studies are not repeated. However, the impacts of new design parameters on F_t are investigated in Subsection 3.2. These include the thickness of the silicone base t_b, canal dimensions (t_1, t_2, t_v, and t_h), chamber aspect ratio r, and chamber shapes and orientation. The tip force is measured according to the common

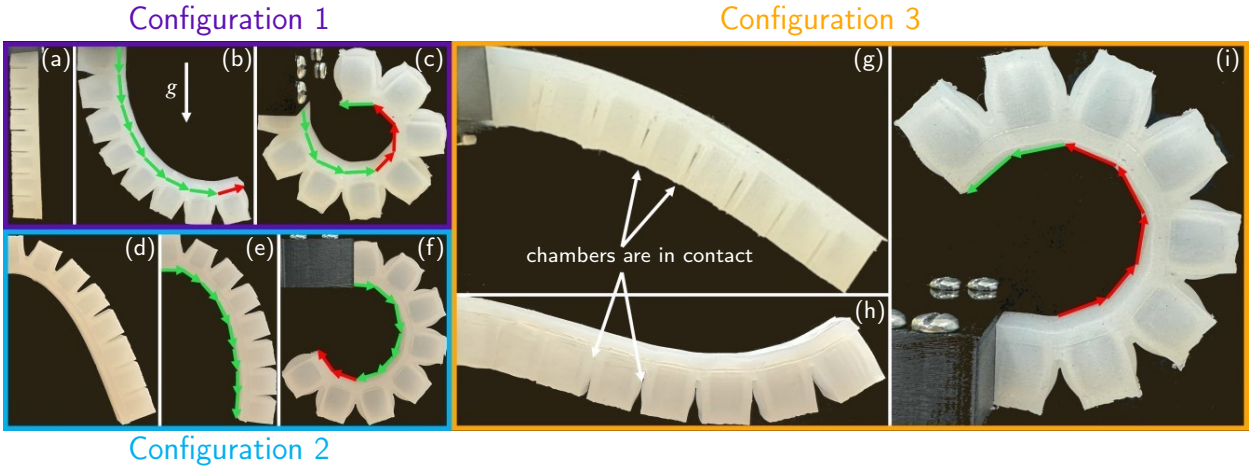

Figure 3: Three different configurations of a PneuNet are shown: In configuration 1 ((a), (b), and (c)), the PneuNet is vertically suspended. In configuration 2 ((d), (e), and (f)), the PneuNet is horizontally mounted with its chambers facing upwards. In configuration 3 ((g), (h), and (i)), the PneuNet is horizontally mounted with its chambers facing downwards. Given the direction of gravity in (b), the tangent vectors to the circular deformation are represented by a green arrow if its direction is positive (with respect to gravity) and by a red arrow if it is negative.

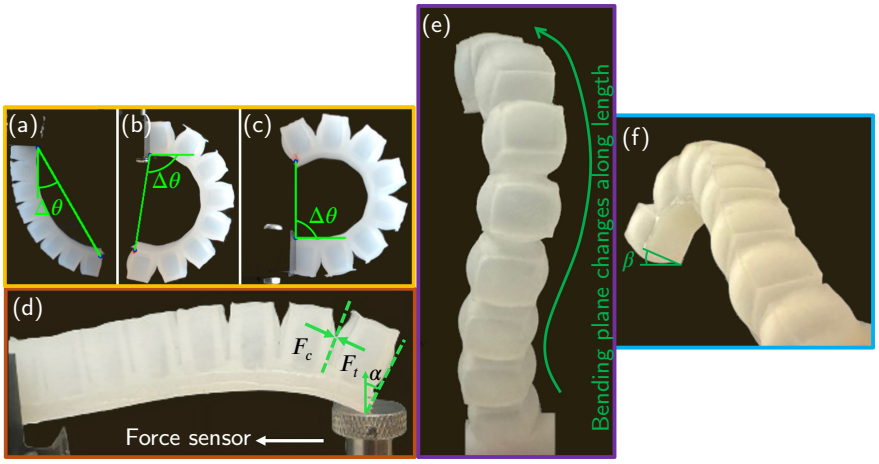

Figure 4: Experimental setups for measuring angular deformation: (a) Configuration 1, (b) Configuration 2, and (c) Configuration 3. (d) Tip force F_t measurement using a force sensor, showing the contact force F_c between the last two chambers and the angle α between F_t and and the edge of the silicone base. (e) Top and (f) side views of a PneuNet actuator highlighting buckling and out-of-plane bending, with the actuator tip forming an angle β relative to the normal of its initial bending plane.

practice [30, 32] by fixing one end of the PneuNet actuator and blocking the other end with a digital force gauge (FK 50, Sauter GmbH) as shown in Fig. 4d.

2.3. Resistance to buckling

One of the main limitations of soft actuators is their restricted force output, which diminishes their effectiveness in applications requiring high force output or exposure to significant external forces. This limitation is often attributed to buckling, which, as described by the authors in [40], arises from axial instability when the actuator is subjected to a force at its blocked tip. Buckling is marked by the onset of irregular bending, where the actuator ceases to bend with a constant curvature and instead exhibits noticeable deformation along its length, as shown in Fig. 4e. Additionally, buckling often causes the actuator tip to slip off and to cease being parallel to the surface that obstructs, as illustrated in

Fig. 4f. In this context, F_t is modeled by considering the instability and buckling issues of the actuator, expressed as follows

$$F_t = \frac{Ph\left(S + S_r/\beta\right)}{l} \tag{5}$$

where h is the distance from the geometric center of the channel cross-section to the strain-limiting layer, S is the cross-sectional area of the air channel, S_r is the solid silicone area, and β is a material constant. This equation is derived by equating the tip force moment $F_t l$ to the pressure-induced bending moment PSh and incorporating internal axial stresses within the silicone body $\frac{PS_r}{\beta}$, which counteract buckling. The material constant β represents the silicone stiffness, contributing significantly to its resistance to buckling. Both Eq. [5] and the experimental findings in [27] demonstrate that buckling resistance improves with a decrease in actuator length, an increase in the airflow cross-sectional area, an increase in the silicone solid cross-sectional area, and greater material stiffness.

Although Eq. 5 is specifically designed for fiber-reinforced SPAs, Subsection 3.3 explores its potential as a guiding tool for evaluating buckling in PneuNet actuators. The premise for this suggestion lies in the structural similarities between fiber-reinforced SPAs and PneuNet actuators. For instance, in PneuNet actuators, the chamber airflow cross-sectional area A_{ch} and the canal airflow cross-sectional area A_t correspond to S in Eq. 5, while the chamber solid cross-sectional area A_{rch} and the canal solid cross-sectional area A_{rt} correspond to S_r. Similarly, e_{ch} and e_t correspond to h.

Inspired by [27], resistance to buckling in PneuNet actuators is investigated, focusing on the impact of various design parameters. To evaluate this resistance, the maximum attainable tip force before buckling occurs, referred to as the buckling force F_b, is recorded. For this purpose, the same measurement setup used to evaluate the tip force (Fig. 4b) is employed, where the PneuNet actuator is fixed at one end and blocked at the other by a force sensor. The moment at which buckling occurs is determined through visual inspection, identified as the point when the PneuNet actuator begins to bend irregularly (see Fig. 4e-f). These results, along with the tip forces and angular deformations, are presented in Section 3.

3. Influence of Design Parameters on the Performance of a PneuNet Actuator

To study the impact of the design parameters on its performance, a rectangular PneuNet actuator, similar to the one depicted in Fig. 2, is considered as a reference. This shape is one of the first proposed [14] and has been extensively studied in the literature [12, 24–26]. The fabricated actuator lacks a strain-limiting layer and, based on dimensions reported in previous studies [17, 28, 30], has a total length of $l = 95$ mm. It features 8 chambers, each with a height of $l_1 = 10$ mm, length of $l_2 = 7$ mm, and width of $l_3 = 9$ mm, separated by 1 mm gaps. The chamber walls have thicknesses of $t_{ch} = 2$ mm and $t_{ch_2} = 2$ mm. The silicone base has a thickness of $t_b = 3$ mm, and the internal canal has dimensions of $t_1 = 2$ mm (height) and $t_2 = 2$ mm (width). The silicone surrounding the canal has horizontal and vertical thicknesses of $t_h = 4$ mm and $t_v = 2$ mm, respectively. The effects of each design parameter on angular deformation, tip force, and buckling resistance are analyzed by varying one parameter at a time while keeping the others constant. For this reason, each actuator is fabricated and tested at least 3 times for each performance metric to ensure no outlier behavior (with an average standard deviation of 4° for the angular deformation, 0.005N for the tip force, and 0.016N for the resistance to buckling). Upon testing, if the standard deviations of the experiments on an actuator exceed these values or if it shows outlier behavior with respect to the general tendency, it is refabricated, and all the experiments are repeated again three times.

3.1. Angular Deformation

Previous studies have demonstrated a nonlinear relationship between the angular deformation $\Delta\theta$ of PneuNet actuators and the thickness of the base t_b [24]. Additionally, $\Delta\theta$ increases with parameters such as the number of chambers n [20, 25], as well as the height l_1 [6, 36] and width l_3 [36] of the chambers, while it decreases with the chamber thicknesses t_{ch} [25] and t_{ch_2} [24] and the gap between chambers t_s [20, 24, 25]. The initial focus of the following subsection is examining whether the influence of these design parameters varies across the three configurations depicted in Fig. 3. Subsequently, the analysis extends to include the overall length of the actuator l and previously unconsidered design parameters: the aspect ratio of the chambers r, the height t_1 and length t_2 of the canal, the vertical t_v and horizontal t_h silicone thicknesses surrounding the canal, and the shape and orientation of the chambers.

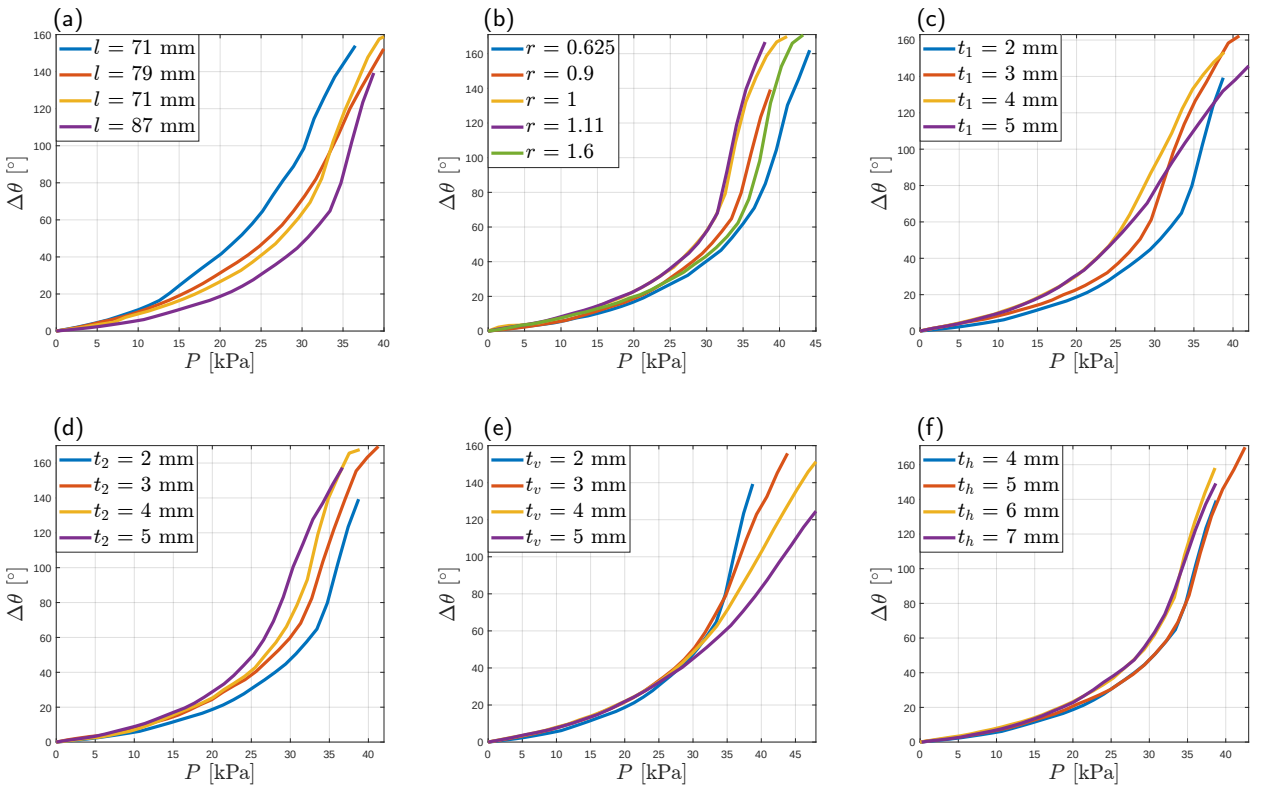

Figure 5: Variation of the angular deformation $\Delta\theta$ as a function of pressure P for different design parameters in configuration 3.

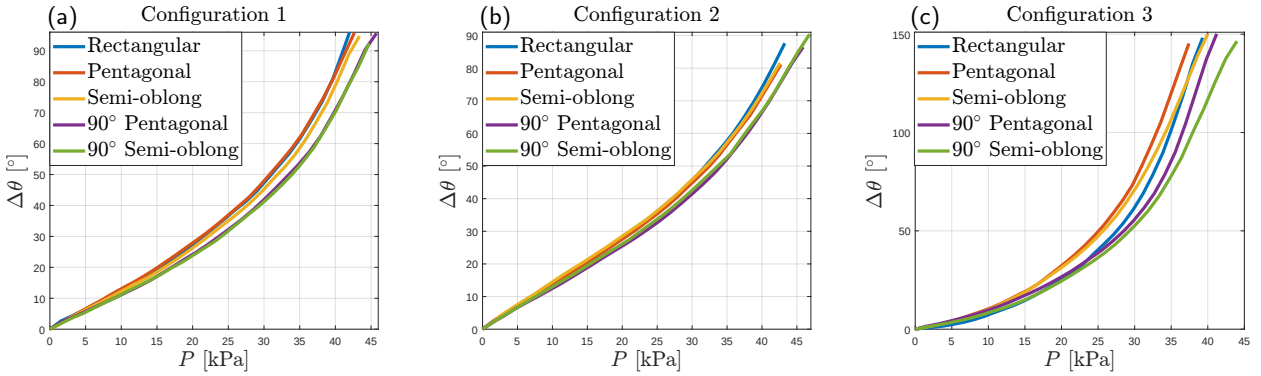

Figure 6: Variation of the angular deformation $\Delta\theta$ as a function of pressure P for different chamber shapes in the three considered configurations.

3.1.1. Impact of Previously Studied Parameters on Various Configurations

This subsection investigates whether the impact of previously examined design parameters (t_{ch}, t_{ch_2}, n, t_s, l_1, l_3, and t_b) varies across different configurations of this PneuNet actuator. To this end, we fabricated actuators with one design parameter varied in each, relative to the reference actuator. Each actuator was pressurized until full bending, and the angular deformation was measured for different values of P in the three configurations. Table 3 shows the average change in $\Delta\theta$ in each configuration.

As shown in Table 3, the impact of design parameters remains consistent across the three configurations, except for t_s. Moreover, each design parameter exhibits a more pronounced impact in configuration 3, especially at $P = 27$ kPa, the pressure at which the actuators bend due to gravity (Fig. 3i). This indicates that the gravitational force amplifies the effect of the design parameters. For instance, while an increase in n generally enhances bending, its effect on $\Delta\theta$ is

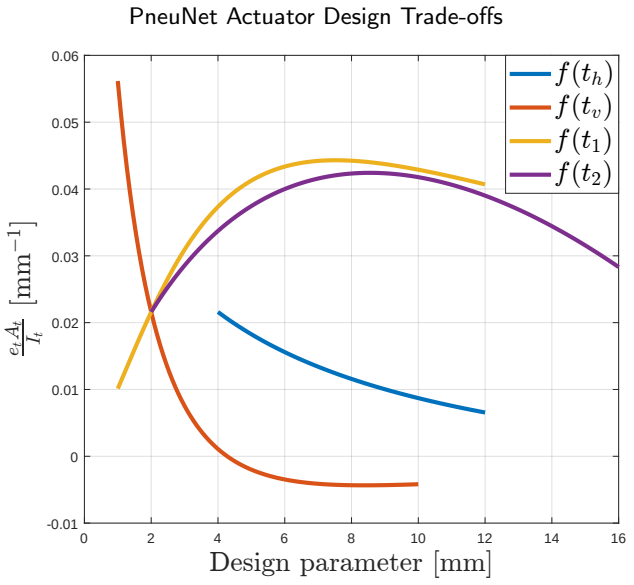

Figure 7: Variation of $\frac{A_t e_t}{I_t}$ as a function of the canal design parameters.

significantly more pronounced in configuration 3 (78%) compared to configurations 1 (21%) and 2 (28%). Under the influence of gravity, an increased number of chambers amplifies the moment due to their weight. Similarly, although an increase in t_s typically reduces angular deformation, in configuration 3, an increase in t_s results in a 40% increase in $\Delta\theta$ due to the larger moment produced by the weight of the chambers, which is further amplified by the increased distance between them.

3.1.2. Impact of actuator length l

Aligning with commonly used actuator lengths in literature [17, 28, 30], the actuator length l was varied between 71 mm and 95 mm. Across all three configurations, a consistent trend is observed: $\Delta\theta$ increases as l decreases. For brevity, Fig. 5a shows $\Delta\theta$ only for configuration 3, while the results for configurations 1 and 2 are provided in the supplementary material [37]. The experimental results obtained here contradict Eq. 2, which suggests that $\Delta\theta$ is proportional to l. This discrepancy arises because Eq. 2 assumes a PneuNet actuator with a strain-limiting layer, which the actuators in this study lack. For actuators with a strain-limiting layer, the flexural rigidity EI in Eq. 2 is determined by this layer [38]. However, in its absence, EI is strain-dependent. In fact, [28] suggests that EI is inversely proportional to l^2. Therefore, $\Delta\theta$ increases when l decreases which corresponds to the results observed in Fig. 5a.

3.1.3. Impact of chamber aspect ratio r

The chamber aspect ratio r is defined as the ratio between the width l_3 and the height l_1 of the chamber. Thus, the impact of the chamber aspect ratio $r = \frac{l_3}{l_1}$ is studied by considering narrow, square, and wide chamber actuators, with r varying between 0.625 and 1.6. Similar to the design parameters presented in Subsection 3.1.1, the impact of r on $\Delta\theta$ is most pronounced in configuration 3, compared to configurations 1 and 2. The results for configurations 1 and 2 are reported in the supplementary material [37]. As shown in Fig. 5b, the narrow actuator ($r = 0.625$) exhibits the lowest angular deformation, whereas the square actuator ($r = 1$) demonstrates the highest. According to the supplemtary material [37], the square actuator consistently shows larger $\Delta\theta$ across all three configurations, whereas the narrow actuator consistently shows the least $\Delta\theta$. These findings suggest that a chamber with a square-shaped cross-section has the best bending abilities.

3.1.4. Canal design parameters t_1, t_2, t_v, and t_h

The study examines the impact of canal dimensions on angular deformation by varying the canal height t_1 and width t_2 between 2 mm and 5 mm. For brevity, results for configurations 1 and 2 are detailed in the supplementary materials [37], while Fig. 5c-d illustrate the angular deformation $\Delta\theta$ for configuration 3. Both design parameters display consistent trends across all three configurations. Specifically, the angular deformation increases with t_1 and peaks at $t_1 = 4$ mm. Conversely, $\Delta\theta$ consistently increases with t_2 in all three configurations.

To explain these results, the ratio $\frac{A_t e_t}{I_t}$, which is proportional to $\Delta\theta$ according to Eq. 2, is evaluated. Here, A_t represents the canal cross-sectional area, I_t denotes the second moment of area of the canal solid cross-sectional area, and e_t is the distance between the virtual neutral axis and the canal airflow center. Note that $A_t = t_1 \times t_2$ and that according to Eq. 1, e_t and I_t depend on t_1, t_2, t_h, and t_v. Starting from here, Fig. 7 presents $\frac{A_t e_t}{I_t}$ as a function of the canal dimensions t_1 and t_2, as well as the dimensions of the surrounding silicone, t_v and t_h. In the absence of a strain-limiting layer (as is the case here), $\frac{A_t e_t}{I_t}$ is strain-dependent. Therefore, the values in Fig. 7 are calculated at rest (no strain), providing the trends of $\frac{A_t e_t}{I_t}$ as a function of the canal design parameters.

Fig. 7 shows a parabolic behavior of $\frac{A_t e_t}{I_t}$ as a function of t_1. Additionally, $\frac{A_t e_t}{I_t}$ exhibits a parabolic trend with t_2, peaking at a higher value than it does with t_1. This explains the results shown in Fig. 5c-d.

The variation of $\Delta\theta$ as a function of the vertical thickness of the silicone surrounding the canal t_v is studied by varying the latter between 2 mm and 5 mm. Fig. 5e shows the evolution of $\Delta\theta$ in configuration 3, with variations in configurations 1 and 2 reported in the supplementary materials [37]. In configuration 3, the impact of t_v on $\Delta\theta$ is most pronounced, showing a clear decline in $\Delta\theta$ as t_v increases, as seen in Fig. 5e. This trend is also confirmed by Fig. 7, where $\frac{A_t e_t}{I_t}$ decreases with increasing t_v.

Finally, increasing the canal horizontal thickness t_h from 4 mm to 7 mm proved to have minimal impact on $\Delta\theta$ with the maximum difference between the five actuators being less than 20%, as shown in Fig. 5f.

3.1.5. Chamber shape

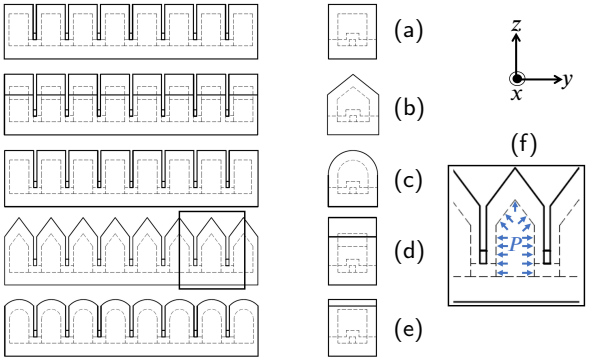

Figure 8: PneuNets with different shapes: (a) rectangular, (b) pentagonal, (c) semi-oblong, (d) pentagonal rotated by 90°, and (e) semi-oblong rotated by 90° with respect to the z-axis. A close-up view (f) shows the pressure distribution along the x-axis in designs (d) and (e) produced by the triangular (circular) cap.

To study the influence of the air distribution on $\Delta\theta$, only the chamber shapes of the PneuNets were varied while keeping other design parameters constant. For this purpose, aside from the rectangular PneuNet, two common shapes were considered: Pentagonal and semi-oblong PneuNet actuators, as illustrated in Fig. 8b-c. The orientation of these chambers was also modified, rotating the pentagonal and semi-oblong chambers by 90° relative to the z-axis (Fig.8d-e), resulting in designs similar to those reported in [6, 22].

Figure 6a-c shows that across all three configurations, the 90° pentagonal and 90° semi-oblong PneuNets exhibit similar $\Delta\theta$, with an average difference of less than 10%. These shapes demonstrate the lowest angular deformations in configurations 1 and 2. However, in configuration 3, their angular deformation is higher than that of the rectangular actuator at low pressure ranges (23 kPa for the 90° pentagonal actuator and 16 kPa for the 90° semi-oblong actuator). Beyond these pressure values, the rectangular actuator exhibits higher angular deformation than both 90° rotated actuators. Although all actuators have the same chamber cross-sectional area, the lower angular deformations of the 90° pentagonal and 90° semi-oblong actuators may be attributed to the presence of a pressure distribution along the z-axis due to their circular and triangular caps (Fig. 8f), rather than having a pressure concentrated along the x-axis.

For the other three actuators (pentagonal, rectangular, and semi-oblong PneuNets), $\Delta\theta$ is similar in configurations 1 and 2, with an average difference not exceeding 5%. In configuration 3, however, the rectangular actuator falls behind, with an angular deformation 17% less than the semi-oblong and 23% less than the pentagonal actuator.

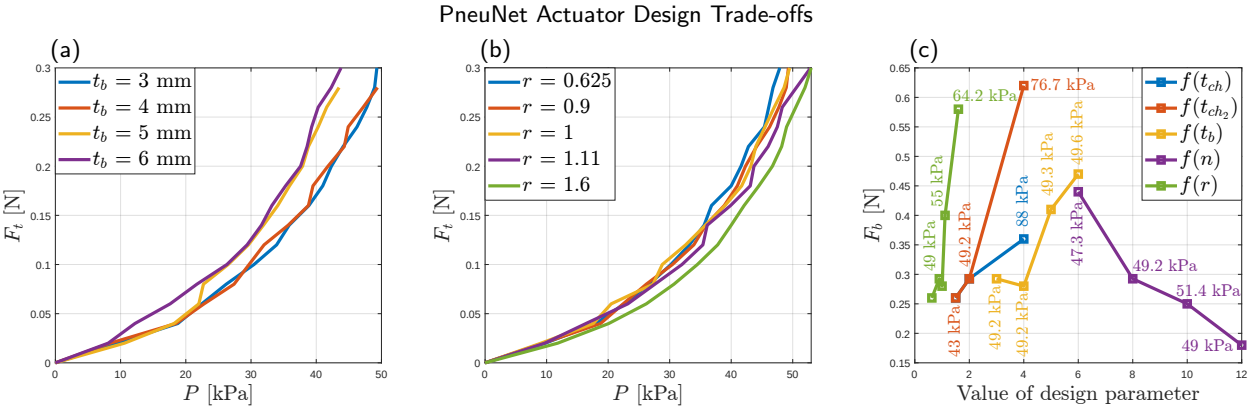

Figure 9: Variation of (a)-(b) the tip force F_t and (c) the buckling force F_b as a function of pressure P for different design parameters.

In conclusion, with all design parameters held constant, the pentagonal and semi-oblong actuators exhibit almost identical $\Delta\theta$, which is slightly superior to that of the rectangular actuator, particularly in configuration 3. Conversely, the 90° pentagonal and 90° semi-oblong PneuNets demonstrate reduced bending abilities.

3.2. Tip force

Another important performance metric of PneuNet actuators is the force exerted at its tip F_t. For a fixed actuation pressure P, F_t increases with the chamber height l_1 [30] and width l_3 [22] while it decreases with the chamber longitudinal t_{ch} [29] and cross-sectional thicknesses t_{ch_2} [22], number of chambers n [23], and the space between the chambers t_s [17]. Furthermore, the analytical model in [17, 25, 29] sugggests that F_t is inversely proportional to the length of the actuator l. To complement the above studies, the current subsection investigates how F_t fluctuates with P when the following design parameters are varied: t_b, r, t_1, t_2, t_v, and t_h.

3.2.1. Thickness of silicone base t_b

As shown in Fig. 9a, increasing the silicone base thickness t_b from 3 mm to 6 mm leads to a 2% to 40% increase in F_t. While t_b increases the chamber A_{rch} and canal A_{rt} solid cross-sectional areas, this outcome is explained by Eq. 4, which indicates that the tip force is proportional to the distance between the chamber's center and and the strain-limiting layer. Our design does not a strain-limiting, but a virtual layer of silicone that remains unchanged in length effectively acts as one. As t_b increases, this virtual layer moves further from the chamber center, enhancing the lever arm and increasing F_t.

3.2.2. Chamber aspect ratio r

According to Fig. 9b, F_t decreases as r increases. Since $r = \frac{l_3}{l_1}$, it follows that F_t is proportional to l_1. This result is consistent with the findings in [30].

3.2.3. Canal design parameters t_1, t_2, t_v, and t_h

The canal height t_1 and width t_2 were varied between 2 mm and 5 mm. Our findings, as reported in the supplementary materials [37], indicate that the tip force F_t increases with an increase in both t_1 and t_2. Notably, the most significant increase in F_t occurs with actuators where $t_1 = 5$ mm and $t_2 = 5$ mm. Under these parameters, F_t is on average 24% higher than that of the reference actuators ($t_1 = 2$ mm and $t_2 = 2$ mm). This increase is attributed to the enlarged canal airflow area, which enhances the pressure moment and consequently the applied force.

3.2.4. Parameters with negligible impact on F_t

In contrast, the silicone vertical t_v and horizontal t_h thicknesses around the canal have negligible impact on F_t. When t_v is varied between 2 mm and 5 mm, the largest recorded variation in F_t is less than 10%. Similarly when t_h is varied between 4 mm and 7 mm, the largest recorded variation in F_t is less than 6%. This can be explained by the fact that t_h and t_v primarily influence the contact between the chambers. However, when measuring F_t, the actuator is blocked at its tip (as shown in Fig. 4d) which forces the chambers into contact during actuation, thereby minimizing the

role of t_h and t_v. Moreover, for actuators sharing the same design parameters, the tip force varies minimally (less than 8%) across the different shapes depicted in Fig. 8.

3.3. Resistance to buckling

In this study, the resistance of PneuNet actuators to buckling is evaluated by measuring the buckling force F_b, defined as the maximum attainable tip force before buckling occurs. An analogy can be drawn with the buckling behavior of beams, where it is well established that shorter beams exhibit greater resistance to buckling. This result is tested through the fabrication of four PneuNet actuators with lengths l of 71 mm, 79 mm, 87 mm, and 95 mm. An inverse relationship between the actuator length and F_b is observed. The values of F_b were measured at 0.36 N, 0.34 N, 0.33 N, and 0.29 N for the actuators of the corresponding lengths. The following subsections focus on the impact of other design parameters on F_b.

3.3.1. Chamber thicknesses t_{ch} and t_{ch_2}

Fig. 9c demonstrates that F_b increases with the chamber longitudinal thickness t_{ch}. Specifically, for $t_{ch} = 4$ mm, F_b reaches 0.36 N at $P = 88$ kPa, which is 64% higher than F_b at $t_{ch} = 1.5$ mm. This enhancement is attributed to the reduced compliance of the PneuNet actuator as the longitudinal thickness increases, which allows more pressure to be utilized for force application rather than for angular deformation.

Similarly, though requiring more pressure, F_b increases by 138% when the chamber cross-sectional thickness t_{ch_2} is increased from 1.5 mm to 4 mm. This result aligns with expectations since the increase in t_{ch_2} enhances the chamber solid cross-sectional area A_{rch}, thus improving its resistance to buckling. This behavior is analogous to that of beams and is consistent with the predictions of Eq. 5.

For both t_{ch} and t_{ch_2}, increasing F_b requires a significant increment in pressure. For instance, with $t_{ch} = 4$ mm ($t_{ch_2} = 4$ mm) F_b is achieved at $P = 88$ kPa ($P = 76.7$ kPa) compared to 43 kPa (40 kPa) for $t_{ch} = 1.5$ mm ($t_{ch_2} = 1.5$ mm).

3.3.2. Thickness of silicone base t_b

The increase in t_b augments the chamber A_{rch} and canal A_{rt} solid cross-sectional areas, thereby enhancing its resistance to buckling. As depicted in Fig. 9f, for the same pressure $P \approx 49$ kPa, there is a substantial increase of 60% in F_b (from 0.29 N to 0.47N) when t_b increases from 3 mm to 6 mm. Therefore, the increase in t_b results in a significant increase in resistance to buckling without necessitating a substantial rise in the applied pressure.

3.3.3. Number of chambers n

Fig. 9c illustrates a significant decrease in the buckling force F_b by approximately 60% as the number of chambers n in the PneuNet actuator increases from 6 to 12, while maintaining a constant actuator length l. This result stems from the actuator's increased compliance due to the increased number of chambers. When the actuator tip is blocked, the chambers are in contact, contributing to the generation of the tip force. However, as the number of chambers increases, the actuator not only becomes more compliant but also experiences an amplified moment due to the chambers interactions. Consequently,the actuation pressure primarily creates deformation rather than force. This leads to increased instability with the rise in n, resulting in a corresponding decrease in F_b. Despite this observation, the pressure at which F_b is reached is relatively constant among the four actuators.

3.3.4. Chamber aspect ratio

To study the impact of the chamber aspect ratio on F_b, the chambers were varied to take narrow, square, and wide shapes, resulting in aspect ratios r ranging from 0.625 to 1.6. All actuators were designed to have the same chamber cross-sectional area A_{rch} and canal cross-sectional area A_{rt} to eliminate the influence of the solid cross-sectional area. Fig. 9c shows a significant increase in F_b for actuators with $r = 1.11$ (38%) and $r = 1.6$ (100%) compared to those with $r = 0.625$, 0.9, and 1. Eq. 5 suggests that the buckling of fiber-reinforced SPAs is influenced by the solid cross-sectional area, airflow area, length of actuator, material used, and distance from the pressure center to the strain-limiting layer. In the present study, the five actuators are made of the same material and have identical length l, solid chamber A_{rch} and canal A_{rt} cross-sectional areas, and chamber A_{ch} and canal A_t airflow cross-sectional areas. Therefore, the only variable left to be investigated is the distance from the chamber centers to strain-limiting layer. However, the actuators fabricated in this paper do not possess a strain-limiting layer. Instead, we calculate the distance e_{ch} between the chamber centers and the position of the virtual neutral axis, as defined by Eq. 1. Considering that the neutral axis position varies with the strain in the actuator, it is determined that at rest (no strain) $e_{ch} = 0.92$ mm for $r = 0.625$, $r = 0.9$, and $r = 1$.

For $r = 1.11$ and $r = 1.6$, e_{ch} is 8% and 30% higher, respectively. Aligning with Eq. 5, this result suggests that e_{ch} significantly increases F_b. Furthermore, as r increases, e_{ch} correspondingly increases, resulting in an elevated F_b.

3.3.5. Design parameters with negligible impact on F_b

The impact of the canal dimensions on the resistance to buckling of the actuator was studied by varying t_1 and t_2 between 2 mm to 5 mm. For both design parameters the variation in F_b is less than 13%. In comparison to the above design parameters, this variation is negligible and might be reasonably associated to fabrication and/or experimental errors. Therefore, we consider that t_1 and t_2 do not have significant impact on F_b.

Similarly, the silicone vertical t_v and horizontal t_h thicknesses around the canal were varied, with t_v ranging from 2 mm to 5 mm and t_h ranging from 4 mm to 7 mm. For both design parameters, the maximum recorded variation in F_b does not exceed 10% and therefore, for the same above reasoning t_h and t_v are considered to have minimal impact on the resistance of the PneuNet actuator to buckling.

Moreover, for actuators sharing the same design parameters but different shapes (Fig. 8), the variation in F_b is less than 10%.

4. Application to grippers

To evaluate how the tested performance metrics translate to one of the most popular applications of PneuNet actuators, namely grippers, five PneuNet grippers with three fingers each were designed. For each gripper, the PneuNet has one of the shapes presented in Fig. 8: rectangular, pentagonal, semi-oblong, 90° pentagonal, and 90° semi-oblong. The grippers are evaluated in two grasping modes: (1) seizing by enveloping the object as shown in Fig.1a and (2) gripping it by the tips of the fingers as shown in Fig. 1b.

4.1. Grasping by enveloping

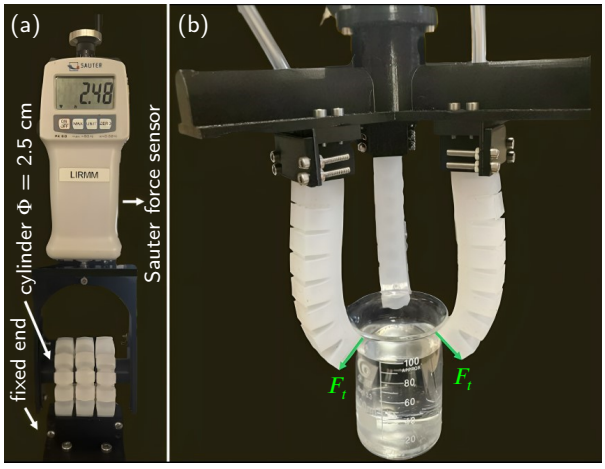

Figure 10: Experimental setups to characterize the grippers in two grasping modes: (a) enveloping and (b) pinching.

One way the grippers seize the object is by enclosing their fingers around it. Inspired by [22], this grasping mode is evaluated by considering a cylinder of diameter Φ. As illustrated in Fig. 10a, the three fingers of the gripper are fixed and actuated at a constant pressure P to envelop the cylinder. The cylinder is then pulled up until the fingers lose their grip around it and the corresponding maximum enveloping force, F_e, is measured using an FK 50, Sauter GmbH force sensor.

The five grippers are first evaluated for a fixed $\Phi = 2.5$ cm and for increasing $P = 20$, 30, and 40 kPa. They are then evaluated for three diameters $\Phi = 2.5$, 5, and 7 cm and a constant actuation pressure $P = 40$ kPa. Each test is repeated three times and the averaged results are shown in Fig. 11a-b.

For a constant $\Phi = 2.5$ cm, Fig. 11a shows that regardless of the gripper shape, the enveloping force F_e increases with the pressure P. Moreover, tha values of F_e are similar at $P = 20$ kPa. However, the enveloping forces become more dispersed when P increases. Furthermore, since this grasping mode requires the PneuNet fingers to encircle the object

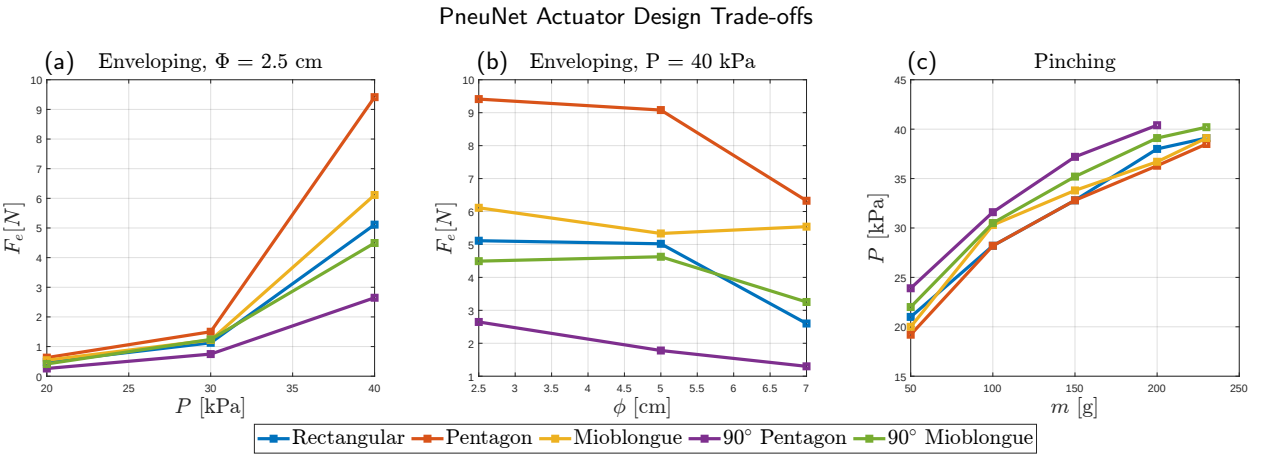

Figure 11: Grasping forces of grippers of different shapes in two grasping modes: (a) Enveloping force F_e vs. pressure P, (b) Enveloping force F_e vs. object diameter Φ, and (c) Required pressure P for grasping vs. object mass m.

by bending around it, the angular deformation $\Delta\theta$ is a deciding factor of F_e. In Subsection 3.1.5, the 90° pentagonal and 90° semi-oblong are found to have the lowest angular deformations. Analogously, these two grippers have the lowest F_e compared to the other ones. For a maximum $P = 40$ kPa, their enveloping forces are 2.64 N and 4.5 N, respectively. On the other hand, the rectangular, pentagonal, and semi-oblong shapes show better grasping capabilities. The pentagonal gripper takes the lead with $F_e = 9.4$ N and the rectangular falls behind with $F_e = 5.1$ N for $P = 40$ kPa.

At a constant P, Fig. 11b illustrates that the enveloping force of the semi-oblong gripper averages around 5.6 N and exhibits the least fluctuation as Φ increases. On the other hand, for all the other grippers, F_e decreases when Φ increases. The pentagonal gripper has the highest F_e for all tested diameters. However, its force drastically decreases from 9.08 N (at $\Phi = 5$ cm) to 6.32 N (at $\Phi = 7$ cm), approaching that of the semi-oblong one. On the other end of the spectrum, the 90° pentagonal gripper has the lowest F_e for all tested diameters. The 90° semi-oblong and rectangular grippers fall in between exhibiting a capability comparable to that of the semi-oblong gripper. For $\Phi = 2.5$ cm and 5 cm, the rectangular gripper outperforms the 90° semi-oblong one. However, at $\Phi = 7$cm, it falls behind, having $F_e = 2.6$ N compared to 3.2 N for the 90° semi-oblong gripper.

4.2. Grasping by pinching

Another gripping mode is holding the object by the tips of the fingers as shown in Fig. 10b. This grasping mode depends on the tip force F_t generated by the PneuNet. It is first evaluated by considering objects of different shapes: a ball, a cube, and a cup. As shown in Table 4, the pressure required by each gripper to lift these objects is almost equal (pressure difference $< 5\%$). Subsection 3.2.4 shows that the tip force of a PneuNet actuator is minimally impacted by the shape of the chamber. The present results agree with the previous conclusion.

Another experiment is conducted where the five grippers attempt to capture a beaker by its rim, as shown in Fig. 10b. The beaker is gradually filled with water to increase its weight, and the pressure P, at which each gripper seizes it, is retained as shown in Fig. 11c.

Except for the 90° pentagonal gripper, which fails to pick up more than 200 g, all the grippers were able to seize the beaker up to a mass of 230 g. The pentagonal, rectangular, and semi-oblong show very similar performance. For these three grippers, the average pressure difference is less than 3% across the five masses. The 90° semi-oblong gripper lags slightly behind, requiring on average 8% more pressure than the other three. The 90° pentagonal gripper ranks last, requiring on average 13% more pressure than the pentagonal one.

Though Fig. 11c shows more disparity in the grippers capabilities compared to the results in Table 4, the differences are not significant enough to contradict the findings of Subsections 3.2.4 and 3.3.5, which state, respectively, that the tip force F_t and the buckling force F_b of a PneuNet actuator is minimally affected by the chamber shape.

5. Discussion

The present study reveals that the influence of the design parameters is most significant when the actuator is horizontally fixed and bends initially against gravity (configuration 3). Moreover, Fig. 12 summarizes the findings of

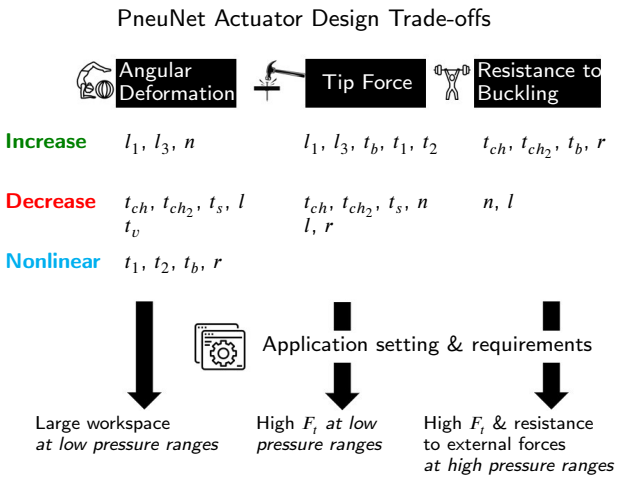

Figure 12: Trends of design parameters to increase the angular deformation, tip force, and resistance to buckling along with the typical application for each performance metric.

Section 3 and serves as a guide for designing PneuNet actuators to meet specific application requirements. It provides a foundation for developing more complex PneuNet designs with superior performance. For example, the angular deformation of the PneuNet actuator increases with the height, width, and number of chambers, while it decreases with the actuator length, chamber thickness, and silicone thickness around the connecting canal. The optimal silicone base thickness and connecting canal dimensions are dependent on the specific design of the PneuNet. Moreover, to increase the angular deformation, the chambers should be square-shaped. Additionally, the space between the chambers should generally be minimized, except in configuration 3, where at high-pressure ranges, the angular deformation increases with a larger space between chambers. The pentagonal, rectangular, and semi-oblong chambers exhibit similar angular deformations, whereas the 90° pentagonal and 90° semi-oblong shapes show reduced performance.

On the other hand, the tip force increases by increasing the canal and chamber cross-sectional areas and the thickness of the silicone base, while all other parameters should be minimized. The thickness of the silicone around the canal and the chamber shape have minimal impact on the tip force.

The PneuNet actuator is more resistant to buckling and can achieve higher forces by increasing the chambers thicknesses, thickness of the silicone base, and chamber aspect ratio. Conversely, the number of chambers and length of the actuator should be decreased. The canal dimensions, the thickness of the silicone around it, and the chamber shape have minimal influence on this performance metric.

Finally, the performance evaluation of grippers with five different shapes indicates that the pentagonal gripper exhibits the best capability to grasp an object by enveloping it. For tip-based grasping, the five grippers demonstrated very comparable behavior.

6. Conclusion

This paper examines the effects of various design parameters on PneuNet actuators, focusing on angular deformation, tip force, and buckling resistance. New parameters, such as chamber aspect ratio, shape, orientation, and connecting canal dimensions, were introduced. Angular deformation was analyzed across three different configurations, revealing configuration-dependent impacts of some design parameters. Additionally, the study introduces the evaluation of buckling resistance in PneuNet actuators, considering the influence of all design parameters. Finally, grippers with various chamber shapes were fabricated and tested in two distinct grasping modes to evaluate their performance.

While this study specifically investigates silicone-based PneuNet actuators, the insights gained regarding the influence of design parameters on performance metrics may extend to actuators made from other soft materials. For instance, a soft material with a higher Young's modulus than silicone would likely exhibit reduced angular deformations, increased tip forces, and enhanced buckling resistance [39], albeit at the cost of requiring higher input pressures. Conversely, a material with a lower Young's modulus would yield greater angular deformations, lower tip forces, and diminished buckling resistance, while demanding lower input pressures. This comprehensive investigation thus provides valuable insights into optimizing PneuNet actuator design for enhanced performance.

References

[1] D. Rus, M. T. Tolley, "Design, fabrication and control of soft robots," *Nature*, vol. 521, no. 7553, pp. 467–475, May 2015. DOI: http://dx.doi.org/10.1038/nature14543

[2] V. K. Venkiteswaran, H. Su, "Extension Effects in Compliant Joints and Pseudo-Rigid-Body Models," *Journal of Mechanical Design*, vol. 138, no. 9, pp. 092302, Sep. 2016. DOI: http://dx.doi.org/10.1115/1.4034111

[3] Y. Liu, J. Hou, C. Li, X. Wang, "Intelligent Soft Robotic Grippers for Agricultural and Food Product Handling: A Brief Review with a Focus on Design and Control," *Advanced Intelligent Systems*, vol. 5, no. 12, pp. 2300233, Dec. 2023. DOI: http://dx.doi.org/10.1002/aisy.202300233

[4] M. Cianchetti, C. Laschi, A. Menciassi, P. Dario, "Biomedical applications of soft robotics," *Nature Reviews Materials*, vol. 3, no. 6, pp. 143–153, May 2018. DOI: http://dx.doi.org/10.1038/s41578-018-0022-y

[5] B. Rother et al., "Tackling the Global Food Crisis: Impact, Policy Response, and the Role of the IMF," International Monetary Fund, Washington, DC, Sep. 2022, IMF Note 2022/004.

[6] J. Lei, Z. Ge, P. Fan, W. Zou, T. Jiang, L. Dong, "Design and Manufacture of a Flexible Pneumatic Soft Gripper," *Applied Sciences*, vol. 12, no. 13, pp. 6306, Jun. 2022. DOI: http://dx.doi.org/10.3390/app12136306

[7] H. Li, H. Bai, Z. Wang, Y. Tan, Y. Tang, "Soft bioinspired pneumatic actuator for adaptive grasping based on direct ink writing method," *Sensors and Actuators A: Physical*, vol. 367, pp. 115041, Mar. 2024. DOI: http://dx.doi.org/10.1016/j.sna.2024.115041

[8] D. Kim, S. R. Baek, M. S. Kim, C. Y. Park, I. H. Lee, "Design and manufacturing process of pneumatic soft gripper for additive manufacturing," *Sensors and Actuators A: Physical*, vol. 370, pp. 115218, May 2024. DOI: http://dx.doi.org/10.1016/j.sna.2024.115218

[9] Y. Wu et al., "A bioinspired multi-knuckle dexterous pneumatic soft finger," *Sensors and Actuators A: Physical*, vol. 350, pp. 114105, Feb. 2023. DOI: http://dx.doi.org/10.1016/j.sna.2022.114105

[10] M. Cao, Y. Sun, J. Zhang, Z. Ying, "A novel pneumatic gripper driven by combination of soft fingers and bellows actuator for flexible grasping," *Sensors and Actuators A: Physical*, vol. 355, pp. 114335, Jun. 2023. DOI: http://dx.doi.org/10.1016/j.sna.2023.114335

[11] H. Li, J. Yao, P. Zhou, X. Chen, Y. Xu, Y. Zhao, "High-force soft pneumatic actuators based on novel casting method for robotic applications," *Sensors and Actuators A: Physical*, vol. 306, pp. 111957, May 2020. DOI: http://dx.doi.org/10.1016/j.sna.2020.111957

[12] S. Nie, L. Huo, H. Ji, Y. Lan, Z. Wu, "Bending deformation characteristics of high-pressure soft actuator driven by water-hydraulics for underwater manipulator," *Sensors and Actuators A: Physical*, vol. 344, pp. 113736, Sep. 2022. DOI: http://dx.doi.org/10.1016/j.sna.2022.113736

[13] Q. Wei, H. Xu, F. Sun, F. Chang, S. Chen, X. Zhang, "Biomimetic fiber reinforced dual-mode actuator for soft robots," *Sensors and Actuators A: Physical*, vol. 344, pp. 113761, Sep. 2022. DOI: http://dx.doi.org/10.1016/j.sna.2022.113761

[14] F. Ilievski, A. D. Mazzeo, R. F. Shepherd, X. Chen, G. M. Whitesides, "Soft Robotics for Chemists," *Angewandte Chemie International Edition*, vol. 50, no. 8, pp. 1890–1895, Feb. 2011. DOI: http://dx.doi.org/10.1002/anie.201006464

[15] B. Mosadegh et al., "Pneumatic Networks for Soft Robotics that Actuate Rapidly," *Advanced Functional Materials*, vol. 24, no. 15, pp. 2163–2170, Apr. 2014. DOI: http://dx.doi.org/10.1002/adfm.201303288

[16] M. S. Xavier, C. D. Tawk, Y. K. Yong, A. J. Fleming, "3D-printed omnidirectional soft pneumatic actuators: Design, modeling and characterization," *Sensors and Actuators A: Physical*, vol. 332, pp. 113199, Dec. 2021. DOI: http://dx.doi.org/10.1016/j.sna.2021.113199

[17] G. Zhong, W. Dou, X. Zhang, H. Yi, "Bending analysis and contact force modeling of soft pneumatic actuators with pleated structures," *International Journal of Mechanical Sciences*, vol. 193, pp. 106150, Mar. 2021. DOI: http://dx.doi.org/10.1016/j.ijmecsci.2020.106150

[18] Y. Zhang, Y. Gan, H. He, "Kinematic analysis of a finger-mimicking pneumatic network actuator consisting of parallelogram-shaped chambers," *Sensors and Actuators A: Physical*, vol. 370, pp. 114865, May 2024. DOI: http://dx.doi.org/10.1016/j.sna.2023.114865

[19] Z. Lv, W. Hao, T. Chen, F. Xiao, Y. Wang, "Copper coils wound finger-like pneumatic actuator with enhanced mechanical output and inductance self-sensing ability," *Sensors and Actuators A: Physical*, vol. 363, pp. 114689, Dec. 2023. DOI: http://dx.doi.org/10.1016/j.sna.2023.114689

[20] S. I. Lee, E. J. Song, Y. I. Yun, H. Moon, H. R. Choi, J. C. Koo, "Soft pneumatic actuator workspace augmentation with synthesis of simplified analytical and numerical subcomponent models," *Sensors and Actuators A: Physical*, vol. 365, pp. 114814, Jan. 2024. DOI: http://dx.doi.org/10.1016/j.sna.2023.114814

[21] F. Wang, Y. Chen, Y. Wang, Z. Liu, Y. Tian, D. Zhang, "A soft pneumatic glove with multiple rehabilitation postures and assisted grasping modes," *Sensors and Actuators A: Physical*, vol. 347, pp. 113978, Nov. 2022. DOI: http://dx.doi.org/10.1016/j.sna.2022.113978

[22] H. K. Yap, H. Y. Ng, C. H. Yeow, "High-Force Soft Printable Pneumatics for Soft Robotic Applications," *Soft Robotics*, vol. 3, no. 3, pp. 144–158, Sep. 2016. DOI: http://dx.doi.org/10.1089/soro.2016.0030

[23] S. Liu, F. Wang, Z. Liu, W. Zhang, Y. Tian, D. Zhang, "A Two-Finger Soft-Robotic Gripper with Enveloping and Pinching Grasping Modes," *IEEE/ASME Transactions on Mechatronics*, Jun. 2020, pp. 1–1. DOI: http://dx.doi.org/10.1109/TMECH.2020.3005782

[24] W. Hu, R. Mutlu, W. Li, G. Alici, "A Structural Optimisation Method for a Soft Pneumatic Actuator," *Robotics*, vol. 7, no. 2, pp. 24, Jun. 2018. DOI: http://dx.doi.org/10.3390/robotics7020024

[25] Z. Liu, F. Wang, S. Liu, Y. Tian, D. Zhang, "Modeling and Analysis of Soft Pneumatic Network Bending Actuators," *IEEE/ASME Transactions on Mechatronics*, vol. 26, no. 4, pp. 2195–2203, Aug. 2021. DOI: http://dx.doi.org/10.1109/TMECH.2020.3034640

[26] W. T. Yang, H. S. Stuart, M. Tomizuka, "Mechanical Modeling and Optimal Model-based Design of a Soft Pneumatic Actuator," 2023 IEEE International Conference on Soft Robotics (RoboSoft), Singapore, Apr. 2023, pp. 1–7. DOI: http://dx.doi.org/10.1109/RoboSoft55895.2023.10122083

[27] Y. Sun, X. Liang, H. K. Yap, J. Cao, M. H. Ang, R. C. H. Yeow, "Force Measurement Toward the Instability Theory of Soft Pneumatic Actuators," *IEEE Robotics and Automation Letters*, vol. 2, no. 2, pp. 985–992, Apr. 2017. DOI: http://dx.doi.org/10.1109/LRA.2017.2656943

[28] G. Alici, T. Canty, R. Mutlu, W. Hu, V. Sencadas, "Modeling and Experimental Evaluation of Bending Behavior of Soft Pneumatic Actuators Made of Discrete Actuation Chambers," *Soft Robotics*, vol. 5, no. 1, pp. 24–35, Feb. 2018. DOI: http://dx.doi.org/10.1089/soro.2016.0052

[29] S. Nikolov et al., "Combined Analytical-FE Modeling of the Deformation Mechanisms and Forces in Soft PneuNets Bending Actuators," 2022 IEEE International Conference on Manipulation, Manufacturing and Measurement on the Nanoscale (3M-NANO), Tianjin, China, Aug. 2022, pp. 301–306. DOI: http://dx.doi.org/10.1109/3M-NANO56083.2022.9941699

[30] P. Polygerinos et al., "Towards a soft pneumatic glove for hand rehabilitation," 2013 IEEE/RSJ International Conference on Intelligent Robots and Systems (IROS), Tokyo, Nov. 2013, pp. 1512–1517. DOI: http://dx.doi.org/10.1109/IROS.2013.6696549

[31] M. S. Xavier, A. J. Fleming, Y. K. Yong, "Finite Element Modeling of Soft Fluidic Actuators: Overview and Recent Developments," *Advanced Intelligent Systems*, vol. 3, no. 2, pp. 2000187, Feb. 2021. DOI: https://dx.doi.org/10.1002/aisy.202000187

[32] E. M. Sierra, J. L. Ordoñez-Avila, "Mathematical Modeling of a Multi-Chamber Pneumatic Soft Actuator," *Actuators*, vol. 11, no. 8, pp. 221, Aug. 2022. DOI: http://dx.doi.org/10.3390/act11080221

[33] M. Yu et al., "Modeling and Analysis of a Composite Structure-Based Soft Pneumatic Actuators for Soft-Robotic Gripper," *Sensors*, vol. 22, no. 13, pp. 4851, Jun. 2022. DOI: http://dx.doi.org/10.3390/s22134851

[34] S. Timoshenko, *Strength of Materials, Part I, Elementary Theory and Problems*, 2nd ed., New York: D. Van Nostrand Company, 1940.

[35] F. P. Beer, R. Johnston, J. T. DeWolf, D. F. Mazurek, "Chapter 5: Statics and Mechanics of Materials," in *Statics and Mechanics of Materials*, McGraw Hill Higher Education, Maidenhead, England, pp. 444–496, 2010.

[36] F. Yang et al., "Design and Optimize of a Novel Segmented Soft Pneumatic Actuator," *IEEE Access*, vol. 8, pp. 122304–122313, 2020. DOI: http://dx.doi.org/10.1109/ACCESS.2020.3006865

[37] Z. Awada, Y. Haddab, M. Gouttefarde, "Supplementary Materials-PneuNet Actuators Design: Trade-offs between Deformation, Force, and Resistance to Buckling," Available at: https://hal.science/hal-04698646

[38] W. Zhou, Y. Li, "Modeling and Analysis of Soft Pneumatic Actuator with Symmetrical Chambers Used for Bionic Robotic Fish," *Soft Robotics*, vol. 7, no. 2, pp. 168–178, Apr. 2020. DOI: https://doi.org/10.1089/soro.2018.0087

[39] A. Garriga-Casanovas et al. , "Optimised Design and Performance Comparison of Soft Robotic Manipulators," 2022 7th International Conference on Mechanical Engineering and Robotics Research (ICMERR), Krakow, Poland, 2022. DOI: https://doi.org/10.1109/ICMERR56497.2022.10097790

[40] Y. Sun et al., "Stiffness Customization and Patterning for Property Modulation of Silicone-Based Soft Pneumatic Actuators," *Soft Robotics*, vol. 4, no. 3, pp. 251–260, Sep. 2017. DOI: https://doi.org/10.1089/soro.2016.004

Table 1
Literature studying the impact of design parameters on the performance of PneuNet actuators and PneuNet grippers. (S.O.: Semi-oblong, Rect.: Rectangular, Hex: Hexagonal, Dec: Decagonal, Vert.: Vertexless, Pent.: Pentagonal, Circ.: Circular)

Ref.	Studied shape	Configuration	Parameters studied on angular deformation evaluation	Parameters studied on tip force evaluation	Evaluated grasping modes
[6]	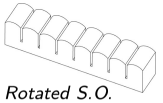 *Rotated S.O.*	Horizontal (bending downward)	Longitudinal thickness, height, and number of chambers. Space between chambers. Thickness of silicone base.	–	Grasping by the tips (Fig. 1b): objects of various mass and shape.
[17]	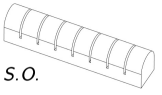 *S.O.*	Horizontal (bending downward)	Lateral thickness of chambers. Space between chambers. Length of actuator.	Lateral thickness of chambers. Space between chambers.	–
[20]	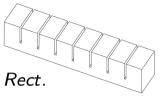 *Rect.*	Horizontal (bending downward)	Number of chambers. Space between chambers. Thickness, shape, and width of silicone base.	–	–
	 *Rect. Hex. Dec. Vert.*		Chamber cross-sectional shape: rectangular, hexagonal, decagonal, and vertexless.	–	–
[22]	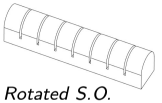 *Rotated S.O.*	–	–	Longitudinal and lateral thicknesses of chambers. Width of chambers. Thickness of base.	Grasping by enveloping (Fig. 1a): cylinders of various diameters.
[23]	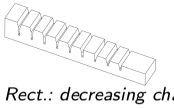 *Rect.: decreasing chamber height*	Horizontal (bending downward)	Number of chambers.	Number of chambers.	Grasping by pinching: objects of various shapes.
[24]	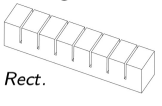 *Rect.*	Horizontal (bending downward)	Lateral thickness and number of chambers. Space between chambers. Thickness of silicone base.		–
	 *Rect. Pent. S.O. Circ.*		Chamber cross-sectional shape: rectangular, pentagonal, semi-oblong, and circular	Chamber cross-sectional shape: rectangular, circular, pentagonal, and semi-oblong.	–
[25]	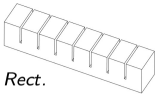 *Rect.*	Horizontal (bending downward)	Longitudinal thickness of chambers. Height, width, and number of chambers. Space between chambers. Thickness of silicone base. Vertical thickness of silicone around canal.	–	–
[26]	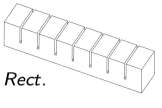 *Rect.*	Vertical (bending upward)	Length of actuator.	Longitudinal thickness of chambers. Height and width of chambers. Length of actuator. Thickness of base.	–

Table 2
Nomenclature of variables used in this paper.

Variable	Definition
P	Actuation pressure
$\Delta\theta$	Angular deformation
F_t	Tip force
F_b	Buckling force
F_p	Tensile force generated by pressure
e_{ch}	Distance between the geometric center of the chamber cross-sectional airflow area and its neutral axis
e_t	Distance between the geometric center of the canal cross-sectional airflow area and its neutral axis
d_{ch}	Position of chamber airflow geometric center
d_t	Position of canal airflow geometric center
l	Actuator length
Δl	Elongation of a chamber when pressurized
$\Delta l'$	Elongation of a canal when pressurized
n	Number of chambers
r	Chamber aspect ratio
l_1	Chamber height
l_2	Chamber length
l_3	Chamber width
t_s	Space between chambers
t_{ch}	Chamber longitudinal thickness
t_{ch_2}	Chamber cross-sectional thickness
t_b	Thickness of silicone base
t_1	Height of canal
t_2	Width of canal
t_h	Horizontal silicone thickness around canal
t_v	Vertical silicone thickness around canal
A_{ch}	Chamber airflow cross-sectional area
A_t	Canal airflow cross-sectional area
A_{rch}	Chamber solid cross-sectional area
A_{rt}	Canal solid cross-sectional area
E	Young's modulus
I_{ch}	Chamber second moment of area
I_t	Canal second moment of area

Table 3
Impact of design parameters on the angular deformation for three configurations.

Reference value	New value	Change in $\Delta\theta$		
		Config. 1	Config. 2	Config. 3
$t_{ch} = 2$ mm	$t_{ch} = 1.5$ mm	+30%	+30%	+58%
$t_{ch_2} = 2$ mm	$t_{ch_2} = 1.5$ mm	+38%	+34%	+79%
$n = 8$	$n = 10$	+21%	+28%	+78%
$t_s = 1$ mm	$t_s = 1.5$ mm	<10%	<10%	+40%
$l_1 = 10$ mm	$l_1 = 8$ mm	-16%	-10%	-20%
$l_3 = 9$ mm	$l_3 = 7$ mm	-19%	-12%	-30%
$t_b = 3$ mm	$t_b = 4$ mm	<10%	<10%	+12%

Table 4
Pressure required by the different grippers to lift a ball, a cube, and a cup. (Pent.: Pentagonal, S.O.: Semi-oblong, Rect.: Rectangular)

Object	Required pressure [kPa]				
	Pent.	S.O.	Rect.	90° Pent.	90° S.O.
Ball	24.6	36	24.1	24.7	25.1
Cube	37.2	36	36	35.1	36.8
Cup	31.2	31.5	31.2	32.4	32